Lawrence Berkeley National Laboratory

LBL Publications

Title

Sharp, high numerical aperture (NA), nanoimprinted bare pyramid probe for optical mapping

Permalink

https://escholarship.org/uc/item/0d97b83w

Journal

Review of Scientific Instruments, 94(3)

ISSN

0034-6748

Authors

Zhou, Junze

Gashi, Arian

Riminucci, Fabrizio

et al.

Publication Date

2023-03-01

DOI

10.1063/5.0104012

Copyright Information

This work is made available under the terms of a Creative Commons Attribution-NonCommercial-NoDerivatives License, available at https://creativecommons.org/licenses/by-nc-nd/4.0/

Peer reviewed

eScholarship.org Powered by the California Digital Library
University of California

Sharp, high numerical aperture (NA), nanoimprinted bare pyramid probe for optical mapping

Junze Zhou[*1], Arian Gashi[1], Fabrizio Riminucci[1], Boyce Chang[1], Edward Barnard[1], Stefano Cabrini[1], Alexander Weber-Bargioni[1], Adam Schwartzberg*[*1], Keiko Munechika*[*2]*

[1]Molecular Foundry, Lawrence Berkeley National Laboratory, 1 Cyclotron Road, Berkeley, CA 94720, USA

[2]HighRI optics, Inc. 5401 Broadway Ter 304, Oakland, CA 94618, USA

The authors to whom correspondence may be addressed: junzezhou@lbl.gov, amschwartzberg@lbl.gov, km@highrioptics.com

1. Abstract

The ability to correlate optical hyperspectral mapping and high resolution topographic imaging is critically important to gain deep insight into the structure-function relationship of nanomaterial systems. Scanning near-field optical microscopy can achieve this goal, but at the cost of significant effort in probe fabrication and experimental expertise. To overcome these two limitations, we have developed a low-cost and high-throughput nanoimprinting technique to integrate a sharp pyramid structure on the end-facet of a single-mode fiber that can be scanned with a simple tuning-fork technique. The nanoimprinted pyramid has two main features: (1) A large taper angle (~70°), which determines the far field confinement at the tip, resulting in a spatial resolution of 275 nm, an effective numerical aperture (NA) of 1.06. (2) A sharp apex with a radius of curvature of ~20 nm, which enables high resolution topographic imaging. Optical performance is demonstrated through evanescent field distribution mapping of a plasmonic nanogroove sample, followed by hyperspectral photoluminescence mapping of nanocrystals using a fiber-in-fiber-out light coupling mode. Through comparative PL mapping on 2D monolayers, we also show a 3-fold improvement in spatial resolution over chemically etched fibers. These results show that the bare nanoimprinted near-field probes provide simple access to spectromicroscopy correlated to high resolution topographic mapping and have the potential to advance reproducible fiber-tip-based scanning near-field microscopy.

2. Introduction

Fiber-based scanning near-field optical microscopy (SNOM) tips have gained popularity for near-field imaging applications due to improved usability over other tip structures. They provide optical and topographic information with relatively high spatial resolutions which can be pushed well beyond the diffraction limit by the addition of plasmonic structures. These tips have improved usability over traditional scattering near-field techniques due largely to two factors: First, the fiber tip-based scanning system uses a quartz tuning fork that has self-sensing detection without an optical feedback mechanism[1], which is ideally suited for light-sensitive near-field measurements where the input of light from laser-based deflection systems can be problematic. Second, the coupling of light through the tip can be designed to be lens-free, allowing for the excitation and collection to be coupled through the same fiber tip[2]. The fiber-based near-field probes have been applied in imaging and spectroscopy of luminescent materials down to single quantum emitters[3–6] with a spatial resolution down to 20 nm[5,7].

The most common fiber probes without plasmonic enhancement are uncoated tapered glass fibers[8] and metalized probes with a small opening aperture[9]. For an uncoated tapered glass fiber, a sharp apex and a small taper angle have been the common approach to achieve high topographic spatial resolution, and an optical spatial resolution on the order of 1 μm. Both the light excitation and collecting could be coupled through the tip, making the technique substrate independent. The techniques to fabricate such tips are chemical etching using hydrofluoric acid (HF)[10], laser-heated pulling[11], or photopolymerization[12,13]. The resulting radius of curvature using these techniques is inconsistent and typically varies between 50 nm and 300 nm. Metalized fiber tips with a smaller aperture size (<50 nm) can be obtained using focused ion beam milling[14–16]. However, this process is time-consuming and has high costs associated with it. The challenge of supplying cheap, robust, and reproducible fiber tips limit the wider use of a relatively straightforward technique that provides topographic and spectroscopic sample information. Hence, an approach to fabricate reproducible and sharp fiber-based tips is in high demand for improving fiber probe-based SNOM.

In this work, we present a solution to the aforementioned challenges by imprinting a high numerical aperture (NA) pyramidal tip on the end of an optical fiber to produce a sharp optical probe through a reproducible and established mass production mechanical lithography process. The pyramidal tip integrated on the facet of fiber is based on the pre-structured silicon mold, which has been proposed by Genolet et al[13]. Here, instead of introducing a guiding structure for the fiber alignment, we simplified the alignment process by using a transparent mold replicated from the silicon, which allows the alignment to be achieved through the fiber-coupled light with the mold in an inverted microscope, which was then followed by the nanoimprinting processed directly on the fiber. To demonstrate the performance of the bare pyramid fiber tip, we first perform a correlated AFM image and evanescent field map of a plasmonic nanogroove sample, demonstrating an optical resolution of 275 nm (effective NA of 1.06). We then demonstrate the capability of hyperspectral photoluminescence (PL) imaging (full spectrum at each point) of two representative sample classes for which this type of near-field imaging is particularly important: Nanocrystal assemblies (Exemplified by lead iodide

perovskite nanocrystals) and 2D semiconductors (Exemplified by monolayer WSe_2). To better understand the light intensity profile in the pyramid tip, the Finite-Difference Time Domain (FDTD) simulations were performed and demonstrated a significantly improved light confinement over conventional etched tips. We demonstrate a 3-fold improvement in resolution when comparing PL maps acquired with the two tip types on the same WSe_2 monolayer flake. Our results demonstrate that the pyramid probe fabricated via this high-throughput nanoimprint method is ideal to perform correlation micro-spectroscopic measurements.

3. Fabrication: Nanoimprinting

The fabrication of the pyramid tip is based on the nanoimprinting method. The fabrication process is shown schematically in Figure 1 (a)[17,18]. The UV photoresist Ormocomp (MicroResist Technologies) is used as the nanoimprinting material, which has a refractive index of 1.52 and is transparent at visible wavelengths. Diluted Ormocomp was dip-coated onto the end facet of a cleaved fiber, single mode fiber (630HP) bought from Thorlabs (630HP). The fiber was mounted onto a piezo stage above the transparent mold and both the template and fiber end facet were visualized through the transparent mold. The mold fabrication is described in the Appendices section, and it is reusable in our process. The fiber core was located by coupling green light into the fiber, then precisely aligned with the pyramid mold by manipulating the piezo stage. UV light (365 nm) was then illuminated through the template to expose the Ormocomp for a curing time of ~3 minutes. The geometry of the imprinted pyramid is shown in Figure 1 (b) and (c). The pyramid is aligned to the center of the fiber core (4 µm diameter) and has a base of 8 µm and a height of 5.6 µm.

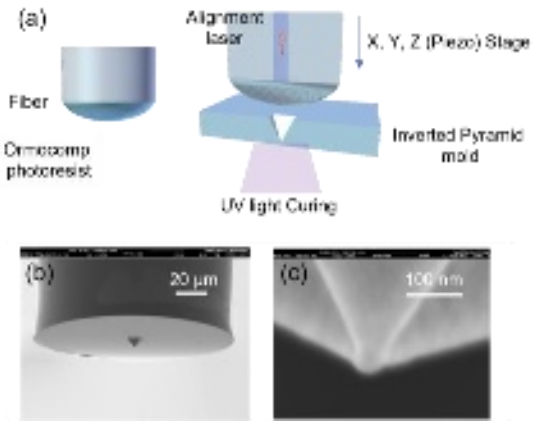

Figure 1. Nanoimprinted pyramid fiber-based tip. (a) Schematic of the nanoimprinting process as described in Ref 9, 10. (b) Tilted SEM view of the imprinted pyramid on Fiber. (c) SEM view of the apex of the pyramid with a curvature size of about 20 nm.

As shown in the zoomed-in view of the tip in Figure 1 (c), the nanoimprinted pyramid has two main advanced features: (1) It has a sharp apex with a radius of curvature of ~20 nm, which determines the imaging resolution in the topographic scan mode. (2) Based on the measured dimension of the base and the height, the pyramid has a large taper angle of ~70°, which we will show to be essential for achieving a confined intensity profile at the tip. As discussed in the following section, the illuminating

light intensity profile at the pyramid tip is more confined than the case of a chemically etched fiber with a smaller taper angle at the apex. This nanoimprinting method is highly reproducible and rapid, making it an ideal system for mass production of near field optical tips. Without any optimization, the fabrication time of one tip is approximately 10 min, which includes the fiber preparation (~1 min), optical alignment (~5 min), UV curing (~3 min) and demolding (~1 min). The production efficiency could be further improved by integrating automated stages for the alignment procedure or parallel imprinting. It is worth noting that because the dimension of the fiber facet is much larger than the pyramid, the tip must be aligned normal to the sample such that the tip contacts the surface before the edge of the fiber. To reduce this tolerance the fiber cladding diameter can be reduced through chemical etching. Here, we have not done this to keep the lithography process fully mechanical.

4. Optical resolution: mapping the near-field distribution using a plasmonic nano-groove

To directly determine the optical resolution of the nanoimprinted tip, we fabricated and imaged a plasmonic nanoantenna, as it has been reported that a bare sharp dielectric tip can be used to convert the evanescent field in the vicinity of a nanostructure to the far-field[19]. Plasmonic nano-groove samples have been extensively applied in photonic circuits[20], plasmonic sensors[21,22] and light absorbers[23] due to their unique linearly polarized plasmonic resonance properties, in a nanoscale gap. In this study, we fabricated a gold nano-groove array sample using template stripping (see Appendices). The total thickness of the gold on the glass substrate is 120 nm, the distance between each groove is 650 nm, the width and depth of each groove is ~15 nm and ~50 nm, respectively. The nano-grooves provide a strong plasmonic resonance that can be excited from below the sample by linearly polarized light with the polarization direction oriented perpendicular to the long axis of the nanogroove (Figure 2 (a), inset). The simulated intensity profile in Figure 2 (e) (See Appendices for the simulation details) confirms that the intensity of the evanescent wave at 15 nm above the sample surface is highly localized in a nanosize dimension of ~60 nm at the vicinity of the nanogroove.

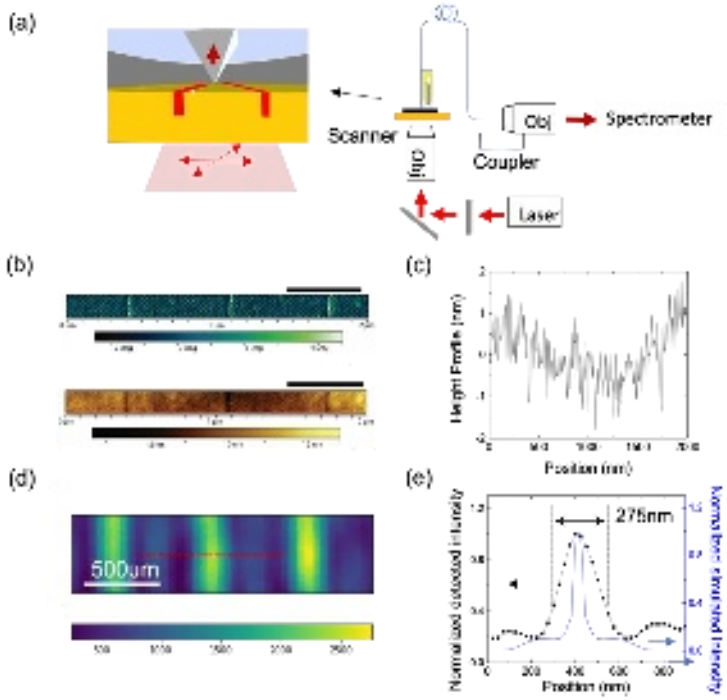

Figure 2. Determination of optical resolution in collection through near-field distribution mapping. (a). Schematic view of the scanning near-field microscope and the measurement configuration. (b). Correlated phase and height images, the scale bar above the images is 500 nm. (c) Height profile along the red dotted line in the height image in (b). (d) Near-field distribution mapping. (e) Intensity profile along the red dotted line in (d) and the simulated intensity profile of a single nanogroove at the position of 15 nm above the sample surface.

Correlated topographic and optical imaging were performed on a scanning near-field optical microscope (AIST-NT) equipped with a shear force head, as shown in Figure 2 (a). A 750 nm excitation laser was coupled to the backside of the nano-groove sample through the bottom objective. The polarization of the laser was aligned perpendicularly to the groove to excite the plasmonic resonance. The nanoimprinted probe was scanned over the sample, where the tip-sample distance was regulated by a tuning fork operating in shear-force mode. When the tip is engaged on the sample surface, light is coupled into the tip and fiber, and ultimately coupled out through a collimating objective lens (×10, NA 0.25) and into a spectrometer (Kymera 328i, Andor). Far-field coupling, or stray light not coupled through the nano-groove, is negligible in the measurement as no transmitted signal was detected when the polarization was rotated to be parallel to the groove.

Figure 2 (b) are the height and phase images obtained by scanning the pyramid tip across the nano-grooves, where the identical spacing of individual nano-grooves is clearly observed. The height profile (Figure 2 c) extracted from the height image along the red dotted line, shows a single deep at the groove position which indicate a single contact point during the scanning process. To be mentioned, the depth of the groove probed by the tip is less deep than the real depth, which is limited by the fact that the aperture size of the tip is larger than the width of the groove. Figure 2 (d) shows the near-field distribution along the gold nano-groove probed by the pyramid tip. A line-scan profile over a single groove (see Figure 2 (e)) yields an optical resolution (OR) of 275 nm, which was obtained using the

standard OR definition based on the full-width at half maximum (FWHM) of the point spread function. For optical mapping with the objective lens, the spatial resolution is determined by the numerical aperture (NA), which can be calculated by: $NA = \frac{\lambda}{2OR}$. While in the fiber probe case, the near-field detection of evanescent waves is through the scattering event, a transfer function is needed for the characterization of the collection SNOM. We calculated the effective NA of the pyramid probe based on the amplitude coupling function (CAF) suggested by S. Bozhevolnyiet al[24].

First, we define the effective NA of the pyramid probe as[25]:

$$NA = \frac{k_{//}}{k_{Air}} \qquad (1)$$

Where $k_{//}$ is in-plane projection of the wave detected by the pyramid tip.

The pyramid probe can be considered as a point-like dipole located inside the tip. The dipole is located at position z_0 and the tip-sample distance is z_t. The transfer function can be expressed as follows[23,24]:

$$H_{xx} = H_{yy} = c_{//} exp\left(-\left(z_0^{//} - z_t\right)\sqrt{k_{//}^2 - k_{air}^2}\right) \qquad (2)$$

$$H_{xz} = c_{\perp} exp\left(-(z_0^{\perp} - z_t)\sqrt{k_{//}^2 - k_{air}^2}\right) \qquad (3)$$

Where H_{xx}, H_{yy} and H_{xz} are the transfer functions of the field the x, y and z directions respectively. $c_{//}$ and $c_{\perp}$ are the contribution of in-plane and out-of-plane components repectively[24].

Here, in the 2D case, we only consider the p-polarized light, and the z component of the field can be neglected since the evanescent field at the nanoslot is confined at the vicinity of the slot. Thus, the field intensity detected by fiber is:

$$I_{tip} = I_0 exp\left(-\left(z_0^{//}\right)\sqrt{k_{//}^2 - k_{air}^2}\right) \qquad (4)$$

From the experiments, we have obtained when $2z_0^{//}NA = 275nm$, the collected intensity drops to e^{-1}, thus $\frac{I_{tip}}{I_0} = e^{-1}$. By combining the formula (1) and (4), we can now obtain the effective NA, which is around 1.06.

We have demonstrated the simple fabrication of the pyramid tip and its high optical spatial resolution near diffraction limit. In the subsequent sections we will show its performance on samples that would be conducive to this measurement technique. We demonstrate the functionality on two low

dimensional optical materials, namely nanocrystal assemblies and 2D materials where the correlation of topographic and spectral information at the exact same position reveals novel functionalities of these material systems.

5. The collection efficiency: PL mapping on nanocrystals

In the previous section we explored the topographic and optical resolution of the bare pyramid probe, next we demonstrate the ability to perform hyperspectral PL mapping on a well understood low dimensional material system of high interest, $CsPbI_3$ perovskite nanocrystals (see Appendices)[26]. Nanocrystal assemblies are becoming increasingly technologically relevant for energy conversion applications. Particularly, Lead halide perovskite nanocrystals have shown fascinating optoelectronic properties with extremely high quantum efficiencies[27], long FRET mediated exciton diffusion[28], and have been used for next generation photovoltaic[29,30] and LED geometries[31]. Device performance often requires understanding the structural relationship between the heterogeneous nanocrystal assembly, both spatially and spectroscopically[32], which requires efficient experimental approaches to characterize these materials down to a few nanocrystals.

The ability to simultaneously collect an optical spectrum at each pixel and topographic information provides critical insight to understand how local material properties and structure result in the macroscopic functionality of a material. Perhaps the most powerful aspect of these fiber-based probes is the ability to both excite and collect through the fiber, removing the need for external optical systems. Additionally, this allows for highly localized excitation and emission, reducing the effect of lateral carrier transport and background signals. As shown in Figure 3 (a), the excitation/collection geometry is simple to achieve with this system. A HeNe laser (633 nm) was coupled into the fiber using the fiber alignment stage as mentioned above, which was then coupled to the sample through the nanoimprinted pyramid. The PL emission of the nanocrystals under the probe was coupled back through the same path. The back-collected spectral information is separated from the excitation source by a dichroic mirror and then sent to a spectrometer.

As shown in Figure 3(b), the nanocrystals have an average diameter of ~15 nm. A hyperspectral PL map featuring both small clusters and a large agglomeration of nanocrystals (See the height map in Figure 3d) is shown in Figure 3 (e). This map has a dimension of 50 pixels × 100 pixels, with a pixel size of 40 nm. At each pixel, the spectrum was obtained by collecting the optical signal for 200 ms with the scanning probe sitting over the same sample position. The plotted map displays the integrated PL intensity in the wavelength range from 650 nm to 750 nm. The spatial resolution of this PL map was estimated on the basis of the optical contrast through the standard 10-90 method[33] as shown in Figure S1 (i). The spatial resolution of this PL map is 280 nm, consistent with the optical resolution obtained in the previous section. The optical resolution was further confirmed to be 285±15 nm, by repeating the hyperspectral optical mapping using different pyramid probes in multiple scans as shown in Figure S1 (See supplementary material).

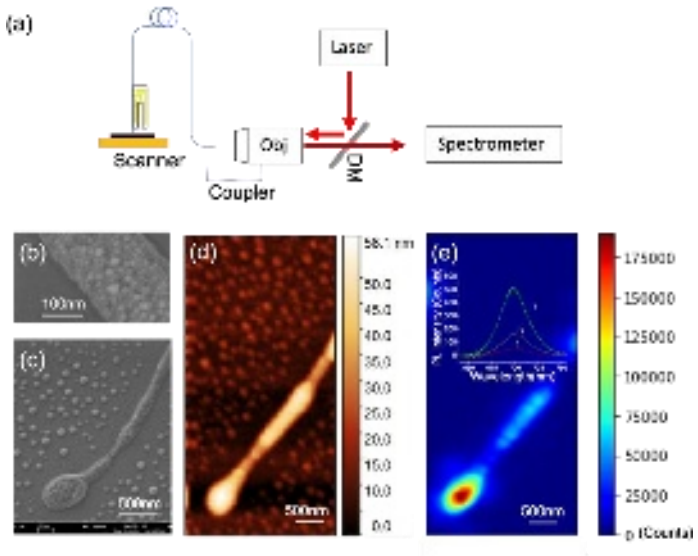

Figure 3. Collection efficiency estimation through PL mapping on limited number of $CsPbI_3$ nanocrystals. (a) Schematic view of the PL measurement configuration. (b) SEM image of the nanocrystals before Al_2O_3 protection layer coating. Correlated SEM image (c), height map (d) and integrated PL map (e). The inset image show in PL spectra selected from the corresponding regions.

Aside from spatial resolution, we also tested the sensitivity/collection efficiency to evaluate the sensitivity of the system. As shown in the PL spectra in the inset of Figure 3 (e), the detected signal in region 3, where the number of nanocrystals is very small as indicated in the correlated SEM image and corresponding AFM scan, has a high signal-to-noise ratio with an integration time of 0.1 s. This provides evidence that the pyramid probe is efficient enough to detect the emission signal from approximately 80 $CsPbI_3$ nanocrystals. These short integration times allow for relatively rapid spectral imaging, and it is also advantageous for chemically sensitive materials[34]. In this PL mapping, the pyramid probe provides similar optical efficiency and spatial resolution of the highest NA oil immersion objectives[28,35] with the advantage of substrate independence and simultaneous topographic

insight. Another example of correlation mapping performed on 2D luminescent materials will be demonstrated in the next section.

6. Comparison spatial resolution: nanoimprinting vs chemical etching

Our aim here is to have a direct comparison of the spatial resolution between a nanoimprinted fiber with a large angle compared to a conventional chemically etched fiber with a narrow angle where the cut-off radius is much further away from the sample. The cut-off radius is defined by the location of the volume where the waveguide mode can no longer be supported by the medium because the dimensions have reduced below half the wavelength of light in that medium[2,36,37]. This means for a probe with a very shallow angle the cut-off radius is much further from the tip apex (and hence the sample) than a probe with a larger taper angle.

To further understand the difference in the excitation profiles of the two types of probes, we performed Finite Element Time Domain (FDTD) simulations to simulate the propagation of linearly polarized light in the probes and calculate the intensity profile at the apex of the probe (See Appendices for simulation details). Figure 4 (a) shows the SEM images of two types of probes and the corresponding light intensity distribution across the probes using the linearly polarized light propagating in the direction towards the apex of the probes. The taper angle of the etched fiber for the simulation is 20°, which is estimated from the SEM view. As shown in the simulated cross-sectional view, the light intensity is confined to a smaller volume at the apex of the pyramid probe than in the case of the etched fiber. The extracted intensity distributions (Figure 4 (d)) at the outputs (5 nm away from the probe) of the probes show that the full-width at half-maximum of the intensity confinement at the output of the pyramid probe is ~3-fold smaller than with the etched probe. This can be explained by the difference in the position of the cut-off at a diameter of approximately half the internal wavelength as indicated by the dotted lines in Figure 4 (a). For the large core diameter, the light propagates in waveguide mode without attenuation. However, further down in the cone, beyond the cut-off, the propagation constant becomes purely imaginary, and the field intensity decays exponentially towards the probe. Thus, the intensity confinement at the probe is mainly determined by the tails of the evanescent wave, which explains the more localized field distribution for the nanoimprinted pyramid probe case versus the etched probe.

2D semiconductors were chosen to confirm these theoretical results as they have atomically sharp edges and extremely low profile surface contours. We conducted comparative testing of PL mapping on monolayer 2D WSe_2[38] with the nanoimprinted pyramid and chemically etched fiber probe. In Figure 4 (b), the sharp change of PL intensity along the edge of the emissive parts and the dotted non-emissive region shows that the optical resolution is around 300 nm (Figure 4 (e)), consistent with the optical resolution obtained in the previous sections. For the chemically etched fiber probe, the optical resolution defined from the hyperspectral PL mapping in Figure 4 (c) is around 800 nm (Figure 4 (f)), which is nearly 3-fold larger than that obtained with the nanoimprinted pyramid As introduced above, the excitation and collection in the PL measurement share the same optical path using the probe.

The spatial resolution of the probe is determined by how large the light spot is at the apex of the probe. Thus, the good agreement between the experimental data and the simulated excitation profiles confirms the advancement of the nanoimprinted pyramid probe in spatial resolution compared to the chemically etched fiber.

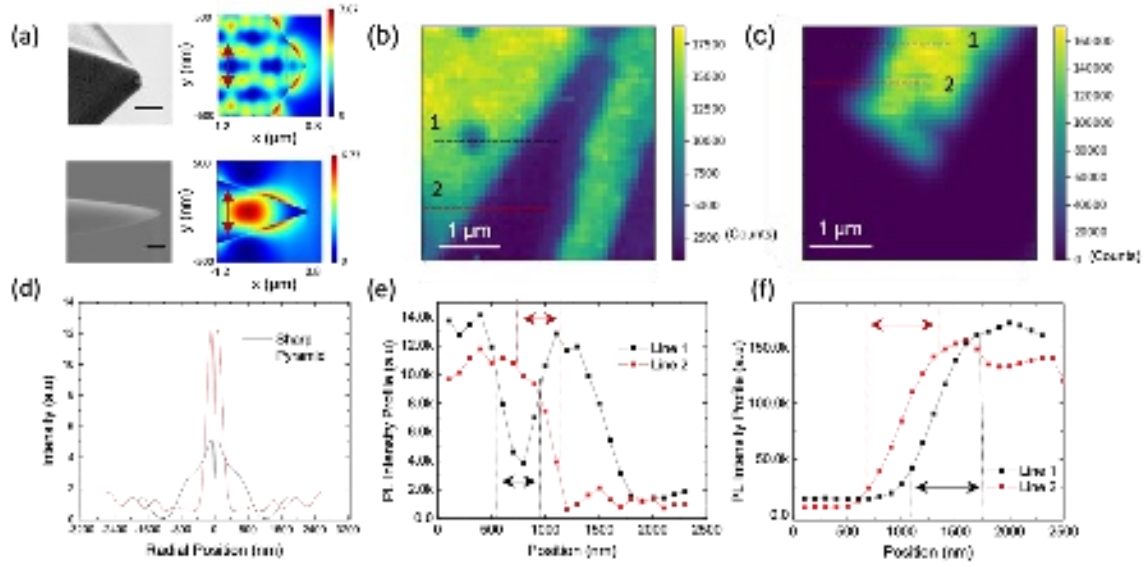

Figure 4. Comparison of optical resolution between the nanoimprinted pyramid probe and the chemically etched probe. (a) SEM images of the nanoimprinted fiber probe and the chemically etched probe and the corresponding intensity distribution inside the pyramid probe and etched fiber probe. The arrow indicates the polarization of the linearly polarized incident light, and the propagation direction is from left to right. The dotted lines are the positions of cut-off radius. Integrated PL map through the pyramid probe (b) and sharp probe (c). (e) and (f) are the corresponding PL intensity profiles. (d) The simulated line profile of the intensity 2 nm away from the probe.

7. Conclusion

In summary, a sharp and high NA near-field probe was fabricated by a high throughput nanoimprinting method. The nanoimprinted pyramid fiber has a radius of curvature of around 20 nm and a large taper angle of 70°. The collection profile was demonstrated by imaging the near-field distribution of the gold nano grooves, which give an optical resolution of light collection of 275 nm, equivalent to an effective NA of 1.06. The high collection efficiency of the bare pyramid probe was then investigated by mapping the limited number of luminescent nanocrystals as well as far-field PL mapping on a WSe_2 monolayer, the pyramid fiber probe can achieve a high signal-to-noise ratio and realized a diffraction-limited optical mapping with a simple optical path setup. A direct comparison between the nanoimprinted pyramid probe and the chemical etched sharp probe proves that the high apex angle is the key feature to achieve a localized collection profile at the probe. The sharp, high NA, nanoimprinted pyramid is highly promising for optical mapping in scanning probe microscope-based

techniques. Furthermore, the small aperture size of the probe provides flexibility to be integrated in space critical systems, such as in a cryogenic chamber.

8. Supplementary Material

Information about the error bar of the optical resolution defined from the PL mapping on $CsPbI_3$ nanocrystals in multiple experiments can be found in supplementary material.

9. Acknowledgments

We thank Ed Wong for technical support, as well as our colleagues at the Molecular Foundry for stimulating discussion and assistance. J. Z thanks Dr. W. Zhao for insightful discussion and direction. Work at the Molecular Foundry was supported by the Office of Science, Office of Basic Energy Sciences, of the U.S. Department of Energy under Contract No. DE-AC02-05CH11231. This research is also partially supported by the Small Business Innovation Research (SBIR) award No. DE-SC0017147.

10. Appendices

Pyramid Mold: The transparent mold is fabricated through the following steps: (1) EBL exposure and development of an electron beam resist (ZEP520A). (2) Pattern transfer into Si_3N_4 by RIE. (3) The undercut of silicon in KOH to form inverted pyramids. (4) Si_3N_4 stripping and completion of the mastermold. (5) Replication of the mastermold into Ormostamp to form pyramids.

Gold Nanogroove fabrication: The gold nanogroove was fabricated by the template stripping method using the HSQ narrow lines through the following steps: (1) Spin coating 2% HSQ at 1000rpm on a polished silicon wafer. (2) The negative resist was exposed by the electron beam lithography using Vistec VB300, creating exposed narrow lines with a thickness of ~50nm and width of ~15nm. (3) Developing the HSQ to obtain the narrow lines, which serves as the template of the nanogrooves. (4) E-beam evaporation of a 120 nm of gold thin film on the templated sample. (5) Place a droplet of ormocomp photoresist on the top of gold and then covering it with a transparent substrate. (6) UV light curing the ormocomp for 90min. (7) Peel the gold off the templated sample with the transparent substrate.

QD synthesis: In a typical reaction, Cs-oleate precursor was first prepared under the following conditions: 0.2 g of Cs_2CO_3 was mixed into a solution of 0.675 ml of oleic acid (OA) and 10 ml of octadecene (ODE) contained in a 50ml three-neck flask. The mixture was heated in N_2 atmosphere at 100˚C and vacuum cycled three times to remove volatile constituents. The temperature was then raised to 110˚C to ensure that Cs_2CO_3 was fully dissolved. 0.087g PbI_2 salt was mixed into a solution of 0.5 ml OA, 0.5 ml Oleylamine and 5 ml ODE in a separate 50 ml three-neck flask. This mixture was similarly cycled through N_2 and vacuum at 100˚C for three rounds. Temperature was then raised to 160˚C, and subsequently, 0.4 ml of Cs-oleate precursor was hot injected (110˚C) into the mixture where a bright red solution can be observed. After 5s, the flask was quenched using an ice bath. Once the

mixture reached room temperature, it was isolated by centrifuging at 10,000 rpm. The $CsPbI_3$ quantum dots were dissolved in toluene and spin coated on Si wafer. These films were protected by coating 20 nm of Al_2O_3 via thermal (40˚C) atomic layer deposition.

WSe_2 monolayer preparation: The WSe_2 crystal was first thinned down by using the tape for a few times until the color of the thin crystal looks reddish. The WSe_2 was then mechanically exfoliated on the SiO_2 substrate. The monolayer region was identified in the optical microscope by checking the color contrast between the substrate and the flake, the thickness of the layer was further confirmed by a single layer thickness of around 0.8 nm in the AFM height scan and the strong PL emission peak at around 750 nm.

FDTD simulation: Simulation of the electromagnetic wave distribution were performed using the commercial Finite-Difference Time-domain (FDTD) method based software and solver package Ansys Lumerical FDTD. Frequency dependent relative permittivity of gold $\varepsilon = \varepsilon_r - i\varepsilon_i$ used for simulation was taken from Johnson and Christy's report[39] and the refractive index of the Ormocomp and SiO_2 were set as n=1.5. 2D simulations were used for the near-field distribution of along the nanogroove and illumination profiles of the probes, since the light responses of the objects in both cases are symmetric in the in-plane direction (perpendicular to the plane of incidence). In both simulations, the objects were placed in the center of a volume with a refractive index n=1. The box was surrounded by 8 layers of stretched coordinate Perfect Matched Layers (PML) on 4 sides to avoid unphysical reflections form the sides. All PMLs were placed far away from the objects to avoid spurious effects coming from a potential interaction between the evanescent waves and the PML. In the nanogroove simulation, 100 layers of mesh were used in the gap of the groove to guarantee accuracy and mesh independent results. A gaussian beam with a waist of ~1μm was sent from the backside of the groove sample (as shown in Figure 2a), and a point detector was placed 15 nm above the sample. The near-field light intensity was recorded by sweeping the source and the detector together with a step size of 5 nm. In the simulation of the light profiles of the probes, a plane wave with electric field component $\mathrm{E}_y = 1\ \mathrm{V/m}$ (see the coordinates in the Figure 4a) was sent from the base of the probes, since the linearly polarized transverse mode is the dominant fundamental mode in the single mode fiber. The light intensity profile was recorded by a monitor placed 2 nm away from the probe. The Mesh type was set as the auto-non-uniform with the min mesh step = 0.1 nm.

8. Reference

(1) Betzig, E.; Trautman, J. K. Near-Field Optics: Microscopy, Spectroscopy, and Surface Modification beyond the Diffraction Limit. *Science* **1992**, *257* (5067), 189–195.

(2) Kim, S.; Yu, N.; Ma, X.; Zhu, Y.; Liu, Q.; Liu, M.; Yan, R. High External-Efficiency Nanofocusing for Lens-Free near-Field Optical Nanoscopy. *Nat. Photonics* **2019**, *13* (9), 636–643.

(3) Ikeda, K.; Matsuda, K.; Saito, H.; Nishi, K.; Saiki, T. Near-Field Spectroscopy of Single Quantum Dots at Room Temperature. *J. Microsc.* **2001**, *202* (Pt 1), 209–211.

(4) Xie, Z.; Lefier, Y.; Suarez, M. A.; Mivelle, M.; Salut, R.; Merolla, J.-M.; Grosjean, T. Doubly Resonant Photonic Antenna for Single Infrared Quantum Dot Imaging at Telecommunication Wavelengths. *Nano Lett.* **2017**, *17* (4), 2152–2158.
(5) Matsuda, K.; Saiki, T.; Nomura, S.; Mihara, M.; Aoyagi, Y.; Nair, S.; Takagahara, T. Near-Field Optical Mapping of Exciton Wave Functions in a GaAs Quantum Dot. *Phys. Rev. Lett.* **2003**, *91* (17), 177401.
(6) Taminiau, T. H.; Moerland, R. J.; Segerink, F. B.; Kuipers, L.; van Hulst, N. F. λ/4 Resonance of an Optical Monopole Antenna Probed by Single Molecule Fluorescence. *Nano Lett.* **2007**, *7* (1), 28–33.
(7) Hosaka, N.; Saiki, T. Near-field Fluorescence Imaging of Single Molecules with a Resolution in the Range of 10 Nm. *J. Microsc.* **2001**, *202* (2), 362–364.
(8) Marcuse, D. *Light Transmission Optics /2nd Edition/*; 1982.
(9) Hecht, B.; Bielefeldt, H.; Pohl, D. W.; Novotny, L.; Heinzelmann, H. Influence of Detection Conditions on near-Field Optical Imaging. *J. Appl. Phys.* **1998**, *84* (11), 5873–5882.
(10) Lambelet, P.; Sayah, A.; Pfeffer, M.; Philipona, C.; Marquis-Weible, F. Chemically Etched Fiber Tips for near-Field Optical Microscopy: A Process for Smoother Tips. *Appl. Opt.* **1998**, *37* (31), 7289–7292.
(11) Valaskovic, G. A.; Holton, M.; Morrison, G. H. Parameter Control, Characterization, and Optimization in the Fabrication of Optical Fiber near-Field Probes. *Appl. Opt.* **1995**, *34* (7), 1215–1228.
(12) Bachelot, R.; Ecoffet, C.; Deloeil, D.; Royer, P.; Lougnot, D. J. Integration of Micrometer-Sized Polymer Elements at the End of Optical Fibers by Free-Radical Photopolymerization. *Appl. Opt.* **2001**, *40* (32), 5860–5871.
(13) Genolet, G.; Despont, M.; Vettiger, P.; Staufer, U.; Noell, W.; de Rooij, N. F.; Cueni, T.; Bernal, M.-P.; Marquis-Weible, F. Micromachined Photoplastic Probe for Scanning near-Field Optical Microscopy. *Rev. Sci. Instrum.* **2001**, *72* (10), 3877–3879.
(14) Pilevar, S.; Edinger, K.; Atia, W.; Smolyaninov, I.; Davis, C. Focused Ion-Beam Fabrication of Fiber Probes with Well-Defined Apertures for Use in near-Field Scanning Optical Microscopy. *Appl. Phys. Lett.* **1998**, *72* (24), 3133–3135.
(15) Bao, W.; Melli, M.; Caselli, N.; Riboli, F.; Wiersma, D. S.; Staffaroni, M.; Choo, H.; Ogletree, D. F.; Aloni, S.; Bokor, J.; Cabrini, S.; Intonti, F.; Salmeron, M. B.; Yablonovitch, E.; Schuck, P. J.; Weber-Bargioni, A. Mapping Local Charge Recombination Heterogeneity by Multidimensional Nanospectroscopic Imaging. *Science* **2012**, *338* (6112), 1317–1321.
(16) Bao, W.; Borys, N. J.; Ko, C.; Suh, J.; Fan, W.; Thron, A.; Zhang, Y.; Buyanin, A.; Zhang, J.; Cabrini, S.; Ashby, P. D.; Weber-Bargioni, A.; Tongay, S.; Aloni, S.; Ogletree, D. F.; Wu, J.; Salmeron, M. B.; Schuck, P. J. Visualizing Nanoscale Excitonic Relaxation Properties of Disordered Edges and Grain Boundaries in Monolayer Molybdenum Disulfide. *Nat. Commun.* **2015**, *6*, 7993.
(17) Calafiore, G.; Koshelev, A.; Allen, F. I.; Dhuey, S.; Sassolini, S.; Wong, E.; Lum, P.; Munechika, K.; Cabrini, S. Nanoimprint of a 3D Structure on an Optical Fiber for Light Wavefront Manipulation. *Nanotechnology* **2016**, *27* (37), 375301.

(18) Calafiore, G.; Koshelev, A.; Darlington, T. P.; Borys, N. J.; Melli, M.; Polyakov, A.; Cantarella, G.; Allen, F. I.; Lum, P.; Wong, E.; Sassolini, S.; Weber-Bargioni, A.; Schuck, P. J.; Cabrini, S.; Munechika, K. Campanile Near-Field Probes Fabricated by Nanoimprint Lithography on the Facet of an Optical Fiber. *Sci. Rep.* **2017**, *7* (1), 1651.

(19) Grosjean, T.; Mivelle, M.; Burr, G. W. Polarization-Dependent Extraction Properties of Bare Fiber Probes. *Opt. Lett.* **2010**, *35* (3), 357–359.

(20) Bozhevolnyi, S. I.; Volkov, V. S.; Devaux, E.; Laluet, J.-Y.; Ebbesen, T. W. Channel Plasmon Subwavelength Waveguide Components Including Interferometers and Ring Resonators. *Nature* **2006**, *440* (7083), 508–511.

(21) Wen, L.; Liang, L.; Yang, X.; Liu, Z.; Li, B.; Chen, Q. Multiband and Ultrahigh Figure-of-Merit Nanoplasmonic Sensing with Direct Electrical Readout in Au-Si Nanojunctions. *ACS Nano* **2019**, *13* (6), 6963–6972.

(22) Eitan, M.; Yifat, Y.; Iluz, Z.; Boag, A.; Hanein, Y.; Scheuer, J. Nano Slot-Antenna Array Refractive Index Sensors: Approaching the Conventional Theoretical Limit of the Figure of Merit. In *Optical Sensors 2015*; SPIE, 2015; Vol. 9506, pp 154–172.

(23) Søndergaard, T.; Novikov, S. M.; Holmgaard, T.; Eriksen, R. L.; Beermann, J.; Han, Z.; Pedersen, K.; Bozhevolnyi, S. I. Plasmonic Black Gold by Adiabatic Nanofocusing and Absorption of Light in Ultra-Sharp Convex Grooves. *Nat. Commun.* **2012**, *3*, 969.

(24) Radko, I. P.; Bozhevolnyi, S. I.; Gregersen, N. Transfer Function and near-Field Detection of Evanescent Waves. *Appl. Opt.* **2006**, *45* (17), 4054–4061.

(25) Greffet, J.-J.; Carminati, R. Image Formation in near-Field Optics. *Prog. Surf. Sci.* **1997**, *56* (3), 133–237.

(26) Imran, M.; Caligiuri, V.; Wang, M.; Goldoni, L.; Prato, M.; Krahne, R.; De Trizio, L.; Manna, L. Benzoyl Halides as Alternative Precursors for the Colloidal Synthesis of Lead-Based Halide Perovskite Nanocrystals. *J. Am. Chem. Soc.* **2018**, *140* (7), 2656–2664.

(27) Dutta, A.; Behera, R. K.; Pal, P.; Baitalik, S.; Pradhan, N. Near-Unity Photoluminescence Quantum Efficiency for All CsPbX3 (X=Cl, Br, and I) Perovskite Nanocrystals: A Generic Synthesis Approach. *Angew. Chem. Int. Ed Engl.* **2019**, *58* (17), 5552–5556.

(28) Penzo, E.; Loiudice, A.; Barnard, E. S.; Borys, N. J.; Jurow, M. J.; Lorenzon, M.; Rajzbaum, I.; Wong, E. K.; Liu, Y.; Schwartzberg, A. M.; Cabrini, S.; Whitelam, S.; Buonsanti, R.; Weber-Bargioni, A. Long-Range Exciton Diffusion in Two-Dimensional Assemblies of Cesium Lead Bromide Perovskite Nanocrystals. *ACS Nano* **2020**, *14* (6), 6999–7007.

(29) Leblebici, S. Y.; Leppert, L.; Li, Y.; Reyes-Lillo, S. E.; Wickenburg, S.; Wong, E.; Lee, J.; Melli, M.; Ziegler, D.; Angell, D. K.; Ogletree, D. F.; Ashby, P. D.; Toma, F. M.; Neaton, J. B.; Sharp, I. D.; Weber-Bargioni, A. Facet-Dependent Photovoltaic Efficiency Variations in Single Grains of Hybrid Halide Perovskite. *Nature Energy* **2016**, *1* (8), 1–7.

(30) Eperon, G. E.; Ginger, D. S. Perovskite Solar Cells: Different Facets of Performance. *Nature Energy* **2016**, *1* (8), 1–2.

(31) Cao, Y.; Wang, N.; Tian, H.; Guo, J.; Wei, Y.; Chen, H.; Miao, Y.; Zou, W.; Pan, K.; He, Y.; Cao, H.; Ke, Y.; Xu, M.; Wang, Y.; Yang, M.; Du, K.; Fu, Z.; Kong, D.; Dai, D.; Jin, Y.; Li, G.; Li, H.; Peng, Q.; Wang, J.; Huang, W. Perovskite Light-Emitting Diodes Based on Spontaneously

Formed Submicrometre-Scale Structures. *Nature* **2018**, *562* (7726), 249–253.
(32) Leonhard, T.; Schulz, A. D.; Röhm, H.; Wagner, S.; Altermann, F. J.; Rheinheimer, W.; Hoffmann, M. J.; Colsmann, A. Probing the Microstructure of Methylammonium Lead Iodide Perovskite Solar Cells. *Energy Technology* **2019**, *7* (3), 1800989.
(33) Wang, C.-F.; Zamkov, M.; El-Khoury, P. Z. Ambient Tip-Enhanced Photoluminescence with 5 Nm Spatial Resolution. *J. Phys. Chem. C* **2021**, *125* (22), 12251–12255.
(34) Protesescu, L.; Yakunin, S.; Bodnarchuk, M. I.; Krieg, F.; Caputo, R.; Hendon, C. H.; Yang, R. X.; Walsh, A.; Kovalenko, M. V. Nanocrystals of Cesium Lead Halide Perovskites (CsPbX3, X = Cl, Br, and I): Novel Optoelectronic Materials Showing Bright Emission with Wide Color Gamut. *Nano Lett.* **2015**, *15* (6), 3692–3696.
(35) Inoué, S. Foundations of Confocal Scanned Imaging in Light Microscopy. In *Handbook of Biological Confocal Microscopy*; Pawley, J. B., Ed.; Springer US: Boston, MA, 1990; pp 1–14.
(36) Bouhelier, A.; Renger, J. B.; Beversluis, M. R. Plasmon-coupled Tip-enhanced Near-field Optical Microscopy. *of microscopy* **2003**.
(37) Novotny, L.; Hecht, B. Principles of Nano-Optics. 2012. https://doi.org/10.1017/cbo9780511794193.
(38) Splendiani, A.; Sun, L.; Zhang, Y.; Li, T.; Kim, J.; Chim, C.-Y.; Galli, G.; Wang, F. Emerging Photoluminescence in Monolayer MoS2. *Nano Lett.* **2010**, *10* (4), 1271–1275.
(39) Johnson, P. B.; Christy, R. W. Optical Constants of the Noble Metals. *Phys. Rev. B Condens. Matter* **1972**, *6* (12), 4370–4379.

Competing interests

The authors declare no competing interests.

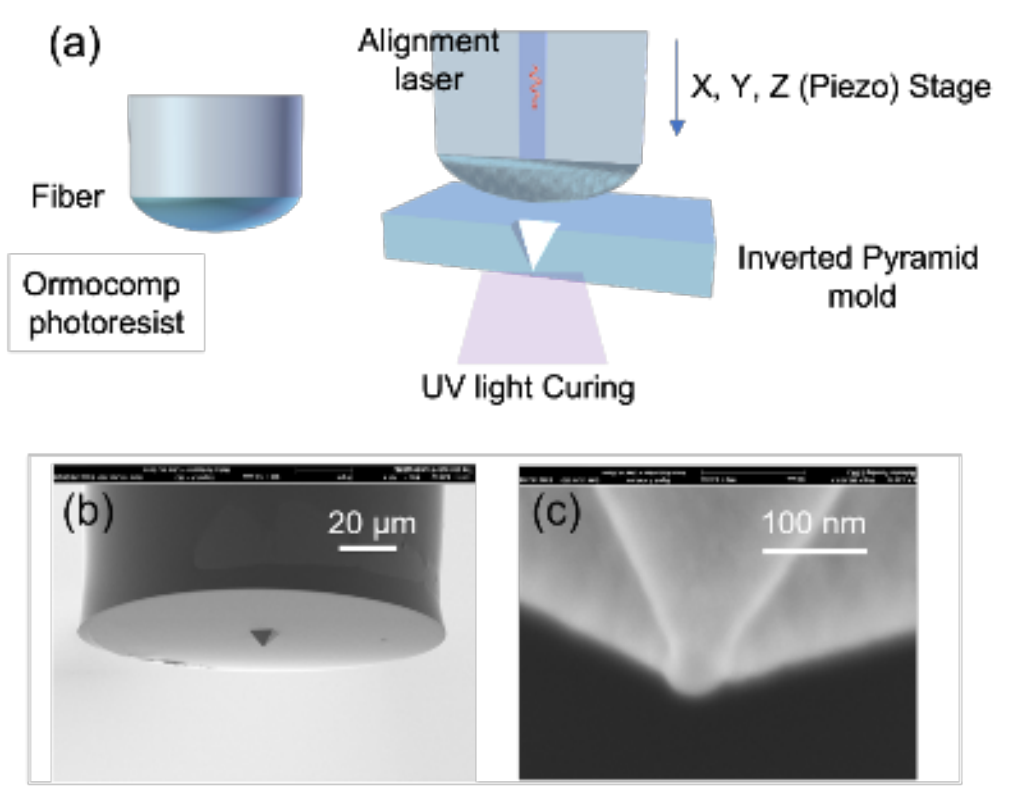
(a)
Alignment laser
X, Y, Z (Piezo) Stage
Fiber
Ormocomp photoresist
Inverted Pyramid mold
UV light Curing
(b)
20 μm
(c)
100 nm

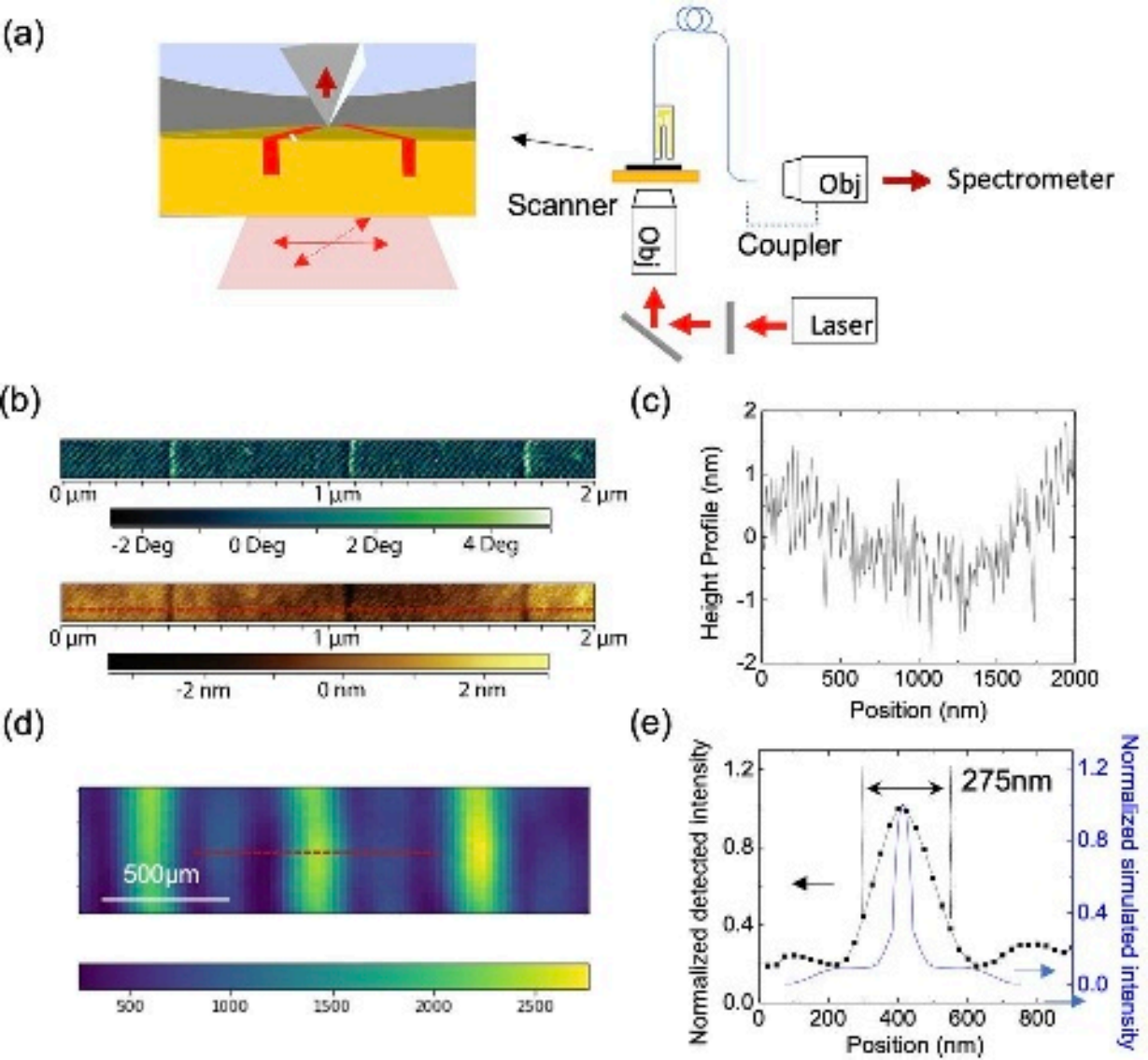
(a)
Scanner
Obj
Obj
Coupler
Spectrometer
Laser
(b)
0 μm
1 μm
2 μm
-2 Deg
0 Deg
2 Deg
4 Deg
0 μm
1 μm
2 μm
-2 nm
0 nm
2 nm
(c)
Height Profile (nm)
Position (nm)
(d)
500μm
500
1000
1500
2000
2500
(e)
Normalized detected intensity
Normalized simulated intensity
275nm
Position (nm)

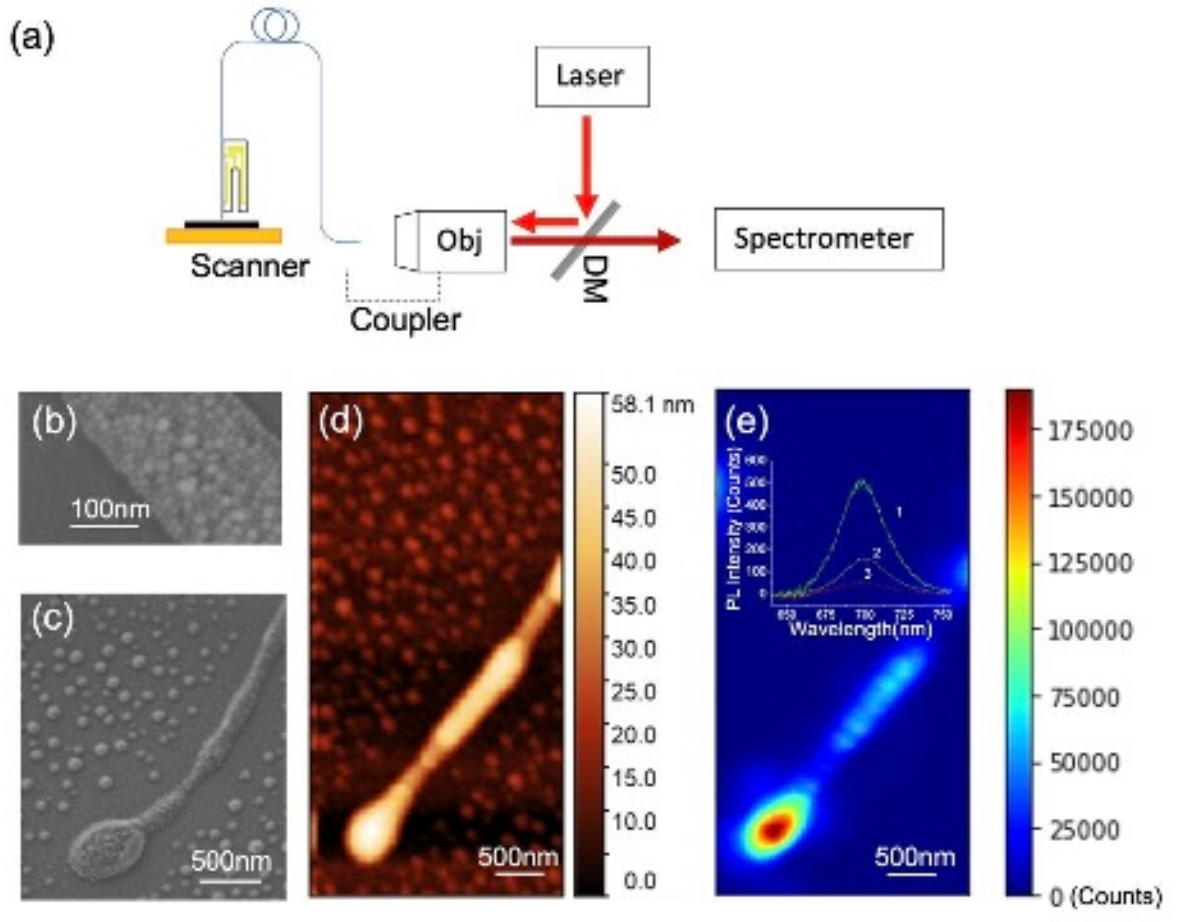
(a)
Laser
Obj
DM
Spectrometer
Scanner
Coupler
(b)
100nm
(c)
500nm
(d)
500nm
58.1 nm
50.0
45.0
40.0
35.0
30.0
25.0
20.0
15.0
10.0
0.0
(e)
PL Intensity (Counts)
Wavelength(nm)
500nm
175000
150000
125000
100000
75000
50000
25000
0 (Counts)

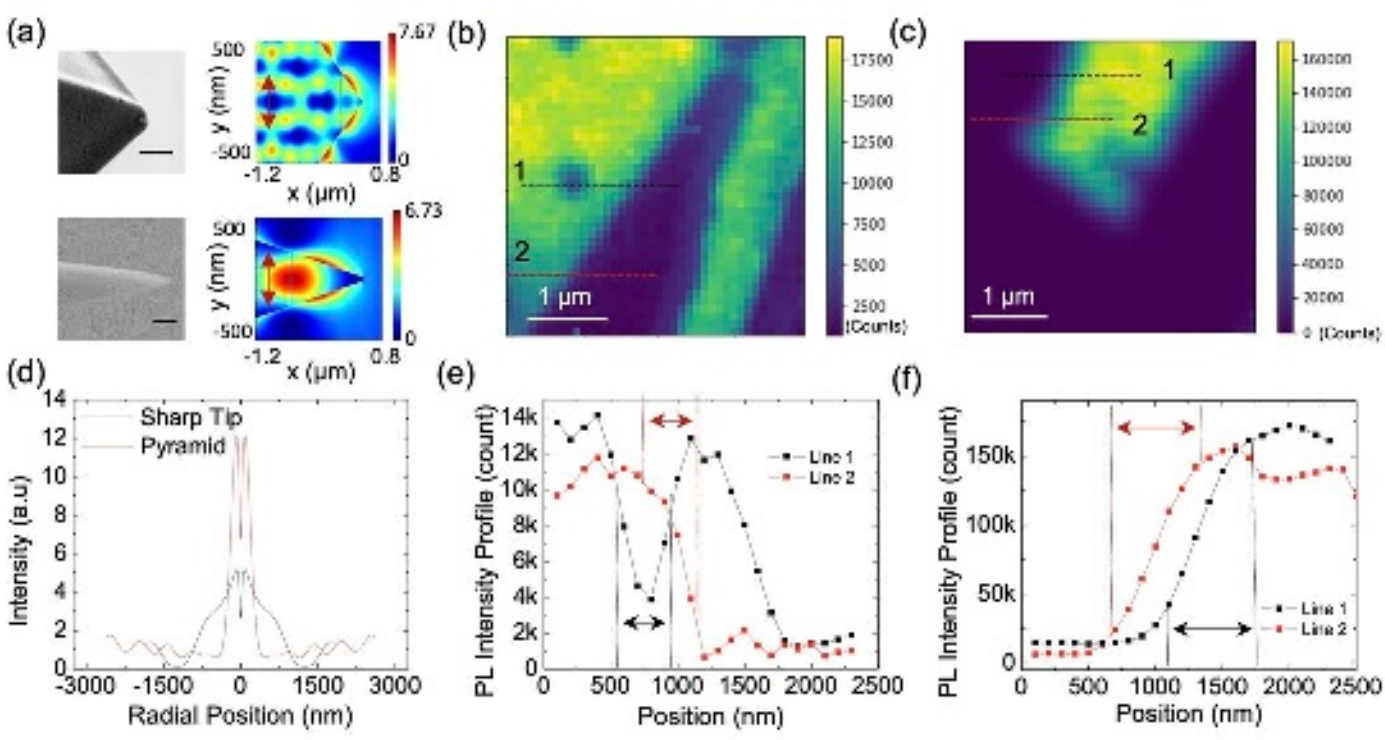
(a)
500
y (nm)
-500
-1.2
x (μm)
0.8
7.67
0
6.73
(b)
1
2
1 μm
17500
15000
12500
10000
7500
5000
2500
(Counts)
(c)
1
2
1 μm
160000
140000
120000
100000
80000
60000
40000
20000
0 (Counts)
(d)
Sharp Tip
Pyramid
Intensity (a.u)
Radial Position (nm)
(e)
PL Intensity Profile (count)
Line 1
Line 2
Position (nm)
(f)
PL Intensity Profile (count)
150k
100k
50k
Line 1
Line 2
Position (nm)